






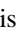






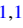
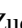




Signature of a Massive Rotating Metal-poor Star Imprinted in the Phoenix Stellar Stream*

Andrew R. Casey^{1,2} , Alexander P. Ji³ , Terese T. Hansen⁴ , Ting S. Li^{3,5,17} , Sergey E. Koposov^{6,7,8} , Gary S. Da Costa^{1,9} , Joss Bland-Hawthorn^{1,10} , Lara Cullinane⁹ , Denis Erkal¹¹ , Geraint F. Lewis¹⁰ , Kyler Kuehn^{12,13} , Douglass Mackey^{1,9} , Sarah L. Martell^{1,14} , Andrew B. Pace⁸ , Jeffrey D. Simpson^{1,14} , and Daniel B. Zucker^{1,15,16} 

¹ Center of Excellence for Astrophysics in Three Dimensions (ASTRO-3D), Australia; andrew.casey@monash.edu

² School of Physics & Astronomy, Monash University, Wellington Road, Clayton 3800, Victoria, Australia

³ Observatories of the Carnegie Institution for Science, 813 Santa Barbara Street, Pasadena, CA 91101, USA

⁴ George P. and Cynthia Woods Mitchell Institute for Fundamental Physics and Astronomy, and Department of Physics and Astronomy, Texas AM University, College Station, TX 77843, USA

⁵ Department of Astrophysical Sciences, Princeton University, Princeton, NJ 08544, USA

⁶ Institute for Astronomy, University of Edinburgh, Royal Observatory, Blackford Hill, Edinburgh EH9 3HJ, UK

⁷ Institute of Astronomy, University of Cambridge, Madingley Road, Cambridge CB3 0HA, UK

⁸ McWilliams Center for Cosmology, Carnegie Mellon University, 5000 Forbes Avenue, Pittsburgh, PA 15213, USA

⁹ Research School of Astronomy and Astrophysics, Australian National University, Canberra, ACT 0200, Australia

¹⁰ Sydney Institute for Astronomy, School of Physics, A28, The University of Sydney, NSW 2006, Australia

¹¹ Department of Physics, University of Surrey, Guildford GU2 7XH, UK

¹² Lowell Observatory, 1400 W Mars Hill Road, Flagstaff, AZ 86001, USA

¹³ Australian Astronomical Optics, Faculty of Science and Engineering, Macquarie University, Macquarie Park, NSW 2113, Australia

¹⁴ School of Physics, University of New South Wales, Sydney, NSW 2052, Australia

¹⁵ Department of Physics & Astronomy, Macquarie University, Sydney, NSW 2109, Australia

¹⁶ Macquarie University Research Centre for Astronomy, Astrophysics & Astrophotonics, Sydney, NSW 2109, Australia

Received 2021 May 17; revised 2021 July 1; accepted 2021 July 9; published 2021 November 1

Abstract

The Phoenix stellar stream has a low intrinsic dispersion in velocity and metallicity that implies the progenitor was probably a low-mass globular cluster. In this work we use Magellan/Magellan Inamori Kyocera Echelle (MIKE) high-dispersion spectroscopy of eight Phoenix stream red giants to confirm this scenario. In particular, we find negligible intrinsic scatter in metallicity ($\sigma([\text{Fe II}/\text{H}]) = 0.04^{+0.11}_{-0.03}$) and a large peak-to-peak range in $[\text{Na}/\text{Fe}]$ and $[\text{Al}/\text{Fe}]$ abundance ratios, consistent with the light element abundance patterns seen in the most metal-poor globular clusters. However, unlike any other globular cluster, we also find an intrinsic spread in $[\text{Sr II}/\text{Fe}]$ spanning ~ 1 dex, while $[\text{Ba II}/\text{Fe}]$ shows nearly no intrinsic spread ($\sigma([\text{Ba II}/\text{H}]) = 0.03^{+0.10}_{-0.02}$). This abundance signature is best interpreted as slow-neutron-capture element production from a massive fast-rotating metal-poor star ($15\text{--}20 M_{\odot}$, $v_{\text{ini}}/v_{\text{crit}} = 0.4$, $[\text{Fe}/\text{H}] = -3.8$). The low inferred cluster mass suggests the system would have been unable to retain supernovae ejecta, implying that any massive fast-rotating metal-poor star that enriched the interstellar medium must have formed and evolved before the globular cluster formed. Neutron-capture element production from asymptotic giant branch stars or magneto-rotational instabilities in core-collapse supernovae provide poor fits to the observations. We also report one Phoenix stream star to be a lithium-rich giant ($A(\text{Li}) = 3.1 \pm 0.1$). At $[\text{Fe}/\text{H}] = -2.93$; it is among the most metal-poor lithium-rich giants known.

Unified Astronomy Thesaurus concepts: [Stellar streams \(2166\)](#)

Supporting material: machine-readable table

1. Introduction

The Milky Way halo is littered with stars that have become gravitationally unbound from their host star cluster (e.g., Ibata et al. 1994; Belokurov et al. 2007; Bonaca et al. 2012). This accretion process produces streams of stars in the Milky Way that lead and trail the progenitor. The Phoenix stellar stream is one recently discovered example, found with the Dark Energy Survey (DES) first data release (Balbinot et al. 2016). The Phoenix stream is at a mean heliocentric distance of 19.1 kpc (Shipp et al. 2019) and spans approximately 8° on the sky (Balbinot et al. 2016). The relatively long arc and on-sky narrow width (54 pc) implies the progenitor system was low mass ($\approx 3 \times 10^4 M_{\odot}$) and had a small velocity dispersion (i.e.,

dynamically cold; Erkal et al. 2016; Shipp et al. 2019; Wan et al. 2020).

These kinematic features are consistent with the Phoenix stream being the tidally disrupted remains of a globular cluster. Low-resolution spectra of Phoenix stream members revealed a metallicity dispersion that is consistent with zero (Li et al. 2019; Wan et al. 2020), confirming a globular cluster origin. However, the mean metallicity of the Phoenix stream is remarkably low ($[\text{Fe}/\text{H}] = -2.7$), making it ~ 0.3 dex more metal-poor than all known surviving globular clusters (Wan et al. 2020). The detailed chemical abundances of stars in an ancient low-mass star cluster can be informative about nucleosynthetic events in the early universe. For this reason, the Phoenix stream represents a unique opportunity to study the formation of ancient globular clusters that are very low mass, and very metal-poor.

In this work we describe high-resolution spectroscopic observations of eight Phoenix stream members and present their detailed chemical abundances. In Section 2, we describe

* This paper includes data gathered with the 6.5 m Magellan Telescopes located at Las Campanas Observatory, Chile.

¹⁷ NHFP Einstein Fellow.

Table 1
Sky Positions and Exposure Times for all Stars Observed

Star	R.A. (hh:mm:ss)	Decl. (hh:mm:ss)	Gaia DR2 Designation	Observed Date	Exp. (minutes)	g (mag)	Slit (arcsec)	S/N 450 nm	S/N 650 nm
Phoenix-1	01:23:48.36	-53:57:27.4	4914426859986001920	2018 Oct 1	50	16.98	0.7	22	38
Phoenix-2	01:24:36.27	-53:40:01.2	4914446067079706624	2019 Oct 19	120	17.65	0.7	12	20
Phoenix-3	01:25:55.15	-53:17:35.1	4914527911976567424	2019 Jul 25	120	17.57	0.7	20	39
Phoenix-6	01:39:20.84	-49:09:11.7	4917862490225433984	2018 Sep 30	90	15.96	1.0	14	28
Phoenix-7	01:42:44.22	-47:29:05.2	4954034292475361280	2018 Oct 1	30	16.28	0.7	25	44
Phoenix-8	01:41:53.37	-47:06:51.6	4954245123830234240	2019 Jul 27	120	17.71	0.7	20	37
Phoenix-9	01:48:16.06	-44:20:53.8	4955727815260641408	2018 Oct 1	40	16.99	0.7	19	34
Phoenix-10	01:51:02.50	-43:02:41.0	4956084950380306816	2018 Sep 30	134	16.64	1.0	23	41

Note. Designations from Wan et al. (2020). S/N has units pixel^{-1} .

the observations that were performed as part of the Southern Stellar Stream Spectroscopic Survey (S^5 ; Li et al. 2019). In Section 3, we summarize our methods (which are expanded upon in Ji et al. 2020) and our results are provided in Section 4. We discuss those results in Section 5 and provide concluding statements in Section 6.

2. Observations

We selected candidate Phoenix stream members based on whether their sky positions and proper motions were consistent with the orbit of the Phoenix stream (Balbinot et al. 2016; Gaia Collaboration et al. 2018; Li et al. 2019; Shipp et al. 2019). We then restricted the candidates to those with $g-r$ colors (Morganson et al. 2018) and apparent magnitudes (at the distance of the stream) that were consistent with a 12 Gyr very metal-poor isochrone (Dotter et al. 2008). We acquired medium-resolution near-infrared spectra at the Ca II triplet of candidate members using the AAOmega spectrograph on the 3.9 m Anglo-Australian Telescope, of which 25 were consistent with stream membership based on their velocities and metallicities (for further details see Wan et al. 2020).

We observed the brightest eight Phoenix stream members between 2018 September 30 and 2019 October 19 with the MIKE spectrograph (Bernstein et al. 2003) on the 6.5 m Magellan Clay telescope at Las Campanas Observatory, Chile. All observations were conducted in good conditions at low airmass (<1.25), with exposure times set to achieve a signal-to-noise ratio (S/N) of 20 per pixel at 400 nm (Table 1). We used the $1.0''$ slit for Phoenix-6 to suit poorer seeing conditions at the time, and the $0.7''$ wide slit for all other Phoenix observations. We used two-by-two on-chip binning and slow readout speed for all observations to reduce read noise. Biases and flat frames were taken in the afternoon, and arc frames were taken throughout the night. We used the `CarPy` reduction pipeline (Kelson 2003) to reduce the data.

We observed most stars in a single epoch. The exceptions were Phoenix-6 and Phoenix-10, which we observed on two different runs. No significant radial velocity differences were present between the two epochs for these stars, so we stacked the observations as if they were conducted in a single night.

3. Methods

We determined the radial velocity of each observation by a cross correlation of each echelle order against a high-S/N rest-frame spectrum of the very metal-poor star HD 122563 (Frebel et al. 2010). The quoted radial velocity is a mean of individual orders, weighted by the inverse variance of individual velocity

estimates (Ji et al. 2020), with barycentric corrections applied. The radial velocities for Phoenix-6 and Phoenix-10 are a weighted average of individual epochs.

We continuum-normalized each echelle order using spline functions with saturated lines masked out, and iterative sigma clipping to down weight other absorption lines. The continuum-normalized spectra from individual orders were then combined, with each resampled pixel weighted by inverse variance, providing a contiguous spectrum from 332–941 nm. The typical S/N per pixel at 400 nm is 20, and 37 at 650 nm (Table 1).

We performed a standard chemical abundance analysis assuming 1D plane-parallel ATLAS model atmospheres (Castelli & Kurucz 2003) and local thermal equilibrium (LTE). The 2017 version of the MOOG radiative transfer code with improved treatment of scattering (Snedden 1973; Sobeck et al. 2011), was used throughout this analysis, wrapped with the SMHR analysis code (Casey 2014). Equivalent widths of unblended atomic lines were measured from the continuum-normalized spectra, allowing for local continuum fitting around each absorption line. Specifically, we used Gaussian profiles to fit absorption lines, and simultaneously fit the parameters of the Gaussian and a straight line continuum function, while iteratively masking out nearby absorption lines that would otherwise bias our model fit. With each iteration we tested if there were nearby absorption lines that could provide better fit by using a Gaussian profile with the same standard deviation as the absorption line of interest (i.e., same spectral resolution), and if so, we excluded the pixels surrounding that nearby absorption feature. Verification tests of this algorithm are shown elsewhere (Casey 2014; Ji et al. 2020).

The stellar parameters were estimated consistently for all high-resolution spectroscopic observations taken for the S^5 survey (Li et al. 2019; Ji et al. 2020). This allows for a consistent comparison of abundances in different stellar streams. Complete details on the methods to estimate stellar parameters are given in Ji et al. (2020), which we summarize here. We estimated effective temperatures using Dartmouth isochrones (Dotter et al. 2008) and de-reddened $g-r$ photometry from the DES (Morganson et al. 2018). Specifically we use 12 Gyr α -element enhanced isochrones with $[\text{Fe}/\text{H}] = -2.5, -1.5, \text{ and } -1.0$. For extinction correction in g and r we adopted the color excess $E(B-V)$ from (Schlegel et al. 1998) and extinction coefficients from the first DES data release (DES Collaboration et al. 2018) (see also Equations (1) and (2) from Ji et al. 2020). Assuming a distance modulus from Shipp et al. (2018), we used the isochrone with the closest predicted de-reddened g -band magnitude and converted the de-reddened $g-r$ color to effective temperature. Uncertainties

Table 2
Stellar Parameters for all Targets

Star	T_{eff} (K)	$\log g$	ν_t (km s^{-1})	[M/H]
Phoenix-1	5088 ± 57	2.15 ± 0.16	1.47 ± 0.19	-2.52
Phoenix-2	5252 ± 66	2.51 ± 0.16	1.64 ± 0.30	-2.67
Phoenix-3	5272 ± 67	2.49 ± 0.16	1.49 ± 0.38	-2.76
Phoenix-6	4905 ± 43	1.64 ± 0.16	2.11 ± 0.59	-2.68
Phoenix-7	4980 ± 45	1.82 ± 0.16	1.58 ± 0.18	-2.62
Phoenix-8	5292 ± 71	2.56 ± 0.17	1.53 ± 0.07	-2.79
Phoenix-9	5153 ± 64	2.20 ± 0.16	1.55 ± 0.27	-2.70
Phoenix-10	5279 ± 68	2.12 ± 0.16	1.80 ± 0.33	-2.93

Note. Note that [M/H] refers to the mean stellar metallicity, derived from Fe II lines (Ji et al. 2020).

from photometry, and the choice of isochrone, are propagated to the uncertainty in temperature (about 50–60 K). We estimated surface gravity $\log g$ from DES photometry (DES Collaboration et al. 2018), with bolometric corrections from Casagrande & Vandenberg (2014), and report a typical uncertainty of 0.16 dex. Uncertainties in distance modulus, photometry, and temperature are propagated to our uncertainties in surface gravity.

Equivalent widths of unblended Fe II lines were used to estimate the remaining stellar parameters. With these equivalent width measurements and fixed T_{eff} and $\log g$, we estimated the microturbulence ν_t by balancing the Fe II abundance with respect to the reduced equivalent width, requiring that the mean Fe II abundance matched the model atmosphere metallicity. We assume α -enhanced atmospheres ($[\alpha/\text{Fe}] = +0.4$), and a model metallicity uncertainty of 0.2 dex for all stars. The stellar parameters are given in Table 2 (see also Figure 1). The photometry and spectroscopic analysis of all Phoenix stars observed (except one) are consistent with being first ascent red giant branch stars (Figure 1). The exception is Phoenix-10, which has stellar parameters that are more consistent with being a red clump star.

Detailed chemical abundances are derived from equivalent width measurements for unblended atomic lines, or by spectral synthesis. Uncertainties in chemical abundances include systematic and statistical uncertainties, including correlations between stellar parameters. Upper limits on abundances are estimated by spectral synthesis, given the stellar parameters, an estimated spectral resolution from nearby absorption lines, and the continuum model. We refer the reader to Appendices B–D of Ji et al. (2020) for full details of how uncertainties are estimated, including the construction of the line list and verification of our equivalent widths and spectral syntheses. In Table 3 we list the chemical abundances for each Phoenix star, which are also shown in Figure 2. Ji et al. (2020) provides the line-by-line abundances and uncertainties for all stream stars observed as part of S^5 .

Using measurements and upper limits of chemical abundances for all observed Phoenix stars, we modeled the intrinsic scatter in abundances for each chemical element. We assumed that the Phoenix stream has an unknown abundance mean μ , some intrinsic scatter σ , and that the observed abundance of each star is drawn from a normal distribution $\mathcal{N}(\mu, \sigma)$. We assumed that the true abundance of each star is not known, and that each observation is a noisy realization of the unknown true abundance. The estimated uncertainty in each abundance measurement includes random and systematic effects. If a star has an upper limit, then we assume that the true abundance for

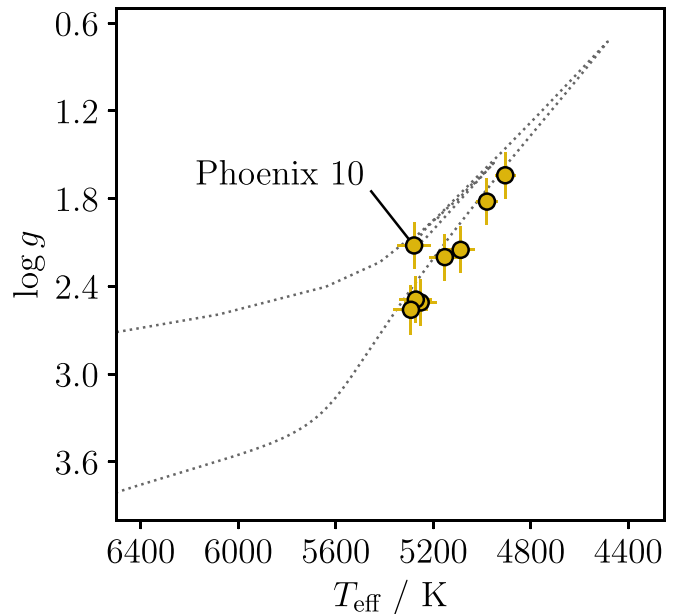


Figure 1. Effective temperature T_{eff} and surface gravity $\log g$ for all Phoenix members observed with Magellan/MIKE, compared to a 12 Gyr metal-poor isochrone (Dotter et al. 2008). The lithium-rich giant star (Phoenix-10) is marked.

that star is not known, and is uniformly drawn between $[X/\text{H}] \sim \mathcal{U}(-4, \hat{u})$, where \hat{u} is the reported limit value. We adopt an improper uniform prior on μ and a uniform prior on $\log \sigma \sim \mathcal{U}(-5, 0)$. We used the Stan (Salvatier et al. 2016; Carpenter et al. 2017) implementation of a Hamiltonian Monte Carlo sampler to draw posterior samples of σ and other nuisance parameters (e.g., the unknown true abundance when only limits are available) for each chemical element.

4. Results

The stellar parameters we report confirm the results by Wan et al. (2020) from low-resolution spectra of 11 red giant branch stars with $S/\text{N} > 10 \text{ pixel}^{-1}$. Our results are based on high-dispersion spectra of eight of those stars. Wan et al. (2020) use equivalent width measurements of the infrared Ca II triplet lines, and the absolute magnitude in the V band, to estimate the stellar metallicity (Carrera et al. 2013). The distance to the stream is used to calculate the absolute magnitude, implying that the calculation is only valid for genuine stream members. Our analysis does not rely on this assumption, and the results between both studies are in excellent agreement.

Wan et al. (2020) estimate the mean metallicity of the stream to be $[\text{Fe}/\text{H}] = -2.70 \pm 0.06$, and we find the mean metallicity to be $[\text{Fe II}/\text{H}] = -2.71 \pm 0.07$. The agreement for both the mean metallicity and its uncertainty is excellent given the different approaches employed to measure metallicities. Similarly, Wan et al. (2020) estimate the intrinsic spread in metallicity in the stream to be $\sigma([\text{Fe}/\text{H}]) = 0.07^{+0.07}_{-0.05}$, and we find $\sigma([\text{Fe II}/\text{H}]) = 0.04^{+0.11}_{-0.03}$. The intrinsic metallicity spread remains consistent with zero, and the relatively high-tailed uncertainty in our posterior distribution is related to our prior on $\log \sigma \sim \mathcal{U}(-5, 0)$.

The chemical abundances for the Phoenix stream are shown in Figure 2, where we compare to a sample of Milky Way stars, and other stream stars with high-resolution spectra from the S^5 program (Li et al. 2019; Ji et al. 2020). The Phoenix stream

Table 3
Summary of Stellar Abundances, Including Differences Due to a 1σ Change in Stellar Parameters

Star	Species	N	ul	$\log \epsilon$	[X/H]	$\sigma_{[X/H]}$	[X/Fe]	$\sigma_{[X/Fe]}$	Δ_T	Δ_g	Δ_v	Δ_M	s_X
Phoenix-1	C-H	2		+6.17	-2.26	0.18	+0.34	0.18	0.13	-0.28	0.01	0.04	0.03
Phoenix-1	C-N	1	<	+5.78	-2.05	...	+0.54
Phoenix-1	O I	1	<	+8.04	-0.65	...	+1.95
Phoenix-1	Na I	2		+3.94	-2.30	0.13	+0.29	0.12	0.05	-0.22	-0.09	-0.02	0.06
Phoenix-1	Mg I	7		+5.38	-2.23	0.05	+0.37	0.06	0.04	-0.07	-0.02	0.01	0.06
Phoenix-1	Al I	2		+3.42	-3.03	0.30	-0.43	0.30	0.08	-0.26	-0.09	0.01	0.30
Phoenix-1	Si I	2		+5.46	-2.04	0.10	+0.55	0.10	0.07	-0.12	-0.04	0.01	0.00
Phoenix-1	K I	2		+3.01	-2.02	0.09	+0.58	0.09	0.04	-0.10	-0.03	-0.00	0.05
Phoenix-1	Ca I	13		+4.03	-2.31	0.04	+0.29	0.05	0.04	-0.08	-0.03	0.00	0.09
Phoenix-1	Sc II	6		+0.56	-2.59	0.15	-0.07	0.17	0.04	0.04	0.01	0.02	0.16
Phoenix-1	Ti I	11		+2.62	-2.33	0.07	+0.27	0.07	0.07	-0.12	-0.03	0.01	0.18
Phoenix-1	Ti II	28		+2.75	-2.19	0.13	+0.33	0.11	0.04	0.11	0.05	0.03	0.17
Phoenix-1	V I	1	<	+1.80	-2.13	...	+0.47
Phoenix-1	V II	1	<	+1.98	-1.95	...	+0.57
Phoenix-1	Cr I	2		+2.61	-3.03	0.08	-0.44	0.08	0.07	-0.11	-0.02	0.01	0.00
Phoenix-1	Fe I	81		+4.90	-2.60	0.04	+0.00	0.00	0.06	-0.10	-0.04	0.01	0.23
Phoenix-1	Fe II	12		+4.98	-2.52	0.16	+0.00	0.00	0.02	0.13	0.00	0.01	0.08
Phoenix-1	Co I	3		+2.61	-2.38	0.11	+0.21	0.12	0.06	-0.07	-0.01	0.00	0.10
Phoenix-1	Ni I	5		+3.66	-2.56	0.08	+0.04	0.09	0.06	-0.10	-0.05	0.00	0.10
Phoenix-1	Cu I	1	<	+2.42	-1.77	...	+0.82
Phoenix-1	Zn I	2		+2.31	-2.25	0.11	+0.35	0.12	0.03	0.03	-0.01	0.01	0.00
Phoenix-1	Sr II	2		+0.51	-2.36	0.24	+0.16	0.22	0.00	0.03	-0.08	-0.04	0.18
Phoenix-1	Ba II	3		-1.41	-3.58	0.16	-1.06	0.14	0.04	0.07	-0.01	0.01	0.10
Phoenix-1	La II	1	<	-0.58	-1.68	...	+0.84
Phoenix-1	Eu II	2	<	-1.43	-1.95	...	+0.57

Note. One star from this table is shown to demonstrate its form and content. The full version is available online.

(This table is available in machine-readable form.)

abundance ratios are comparable to the Milky Way halo in most element abundances. Note the small spread in most abundances relative to other streams, particularly Elqui, which is of a comparable overall mean metallicity.

We show the posterior distribution for intrinsic scatter in each chemical element in Figure 3. The level of intrinsic scatter varies per element, with some elements being consistent with no scatter (e.g., Fe II, Ba II), while others exhibit large and significant scatter (e.g., Sr). Before discussing the element with the most significant scatter (Sr), we provide some context here to clarify how to interpret Figure 3. The posterior in $\sigma([\text{Mn I}/\text{H}]) = 0.05^{+0.35}_{-0.04}$ suggests a long high-end tail, as judged by the high +0.35 positive uncertainty, but this is informed by just two measurements and one upper limit. It is clear at the high end we are only recovering the prior $\log \sigma \sim \mathcal{U}(-5, 0)$, and we cannot confidently rule out large intrinsic scatter given the data. This argument also applies to K (positive uncertainty of +0.25 dex), where only three measurements and five upper limits exist.

Al I provides another example to clarify interpretation. The peak-to-peak abundance range in $[\text{Al I}/\text{H}]$ is large (≈ 0.8 dex; or 1 dex in $[\text{Al I}/\text{Fe}]$) but the reported intrinsic scatter in $[\text{Al I}/\text{H}]$ is low: $\sigma([\text{Al I}/\text{H}]) = 0.06^{+0.23}_{-0.04}$. This is because the estimated uncertainties on individual Al I measurements is larger than other elements, making the distribution of values consistent with very little intrinsic scatter, and in line with the quoted uncertainties. For these reasons, the peak-to-peak range of values and the estimated intrinsic spread are informative in slightly different ways. A handful of other elements show mild evidence of nonzero intrinsic scatter: Na (1σ), K (1.5σ), Ca (2.1σ), and Cr (1.3σ). Even among the most significant of

these, Ca, the actual level of intrinsic scatter is still low, $\sigma([\text{Ca I}/\text{H}]) = 0.13^{+0.12}_{-0.06}$, particularly for globular clusters.

The element with the largest estimated intrinsic scatter is Sr, with $\sigma([\text{Sr II}/\text{H}]) = 0.38^{+0.33}_{-0.21}$. The peak-to-peak range of $[\text{Sr II}/\text{H}]$ values is a little more than ≈ 1 dex, but the uncertainties on individual measurements are many times smaller than this range, implying some level of intrinsic scatter in the stream. Indeed, some stars are relatively Sr-rich, with $[\text{Sr}/\text{Fe}] \sim +0.2$ at $[\text{Fe}/\text{H}] \sim -2.6$. Contrast this with Ba, another neutron-capture element that also has strong absorption lines in metal-poor stars. Naively we might predict the spread in Ba and Sr to be comparable given the individual abundance uncertainties. Instead we find that the mean $[\text{Ba II}/\text{H}]$ is very low ($[\text{Ba}/\text{Fe}] \sim -1$) and the stream has negligible intrinsic scatter for this element. In comparison, the abundance ratios of $[\text{Sr II}/\text{H}]$ show a reasonably large spread ($\gtrsim 1$ dex) and are inconsistent with zero scatter at the $\approx 2\sigma$ level. We show the spectral fits of Ba and Sr transitions in Figure 4.

The $[\text{Sr II}/\text{H}]$ abundance ratios we measure show no correlations with stellar parameters that would be consistent with departures from local thermodynamic equilibrium (LTE) or other missing systematic effects. Indeed, Hansen et al. (2013) estimate the non-LTE departure coefficients for metal-poor ($[\text{Fe}/\text{H}] \approx -2.8$) giants to be $< \pm 0.05$ dex for the 407.77 nm absorption line used in this work, and at most 0.2 dex across all lines (Andrievsky et al. 2011).¹⁸ We

¹⁸ The non-LTE correction for the 421.55 nm Sr II line, a line that we used in this work, is not computed by Hansen et al. (2013) due to blended Fe lines that affect the metal-rich stars in that work. In this work we find no significant difference in abundance between the 407.77 and 421.55 nm lines, of which the former has no significant correction due to non-LTE effects.

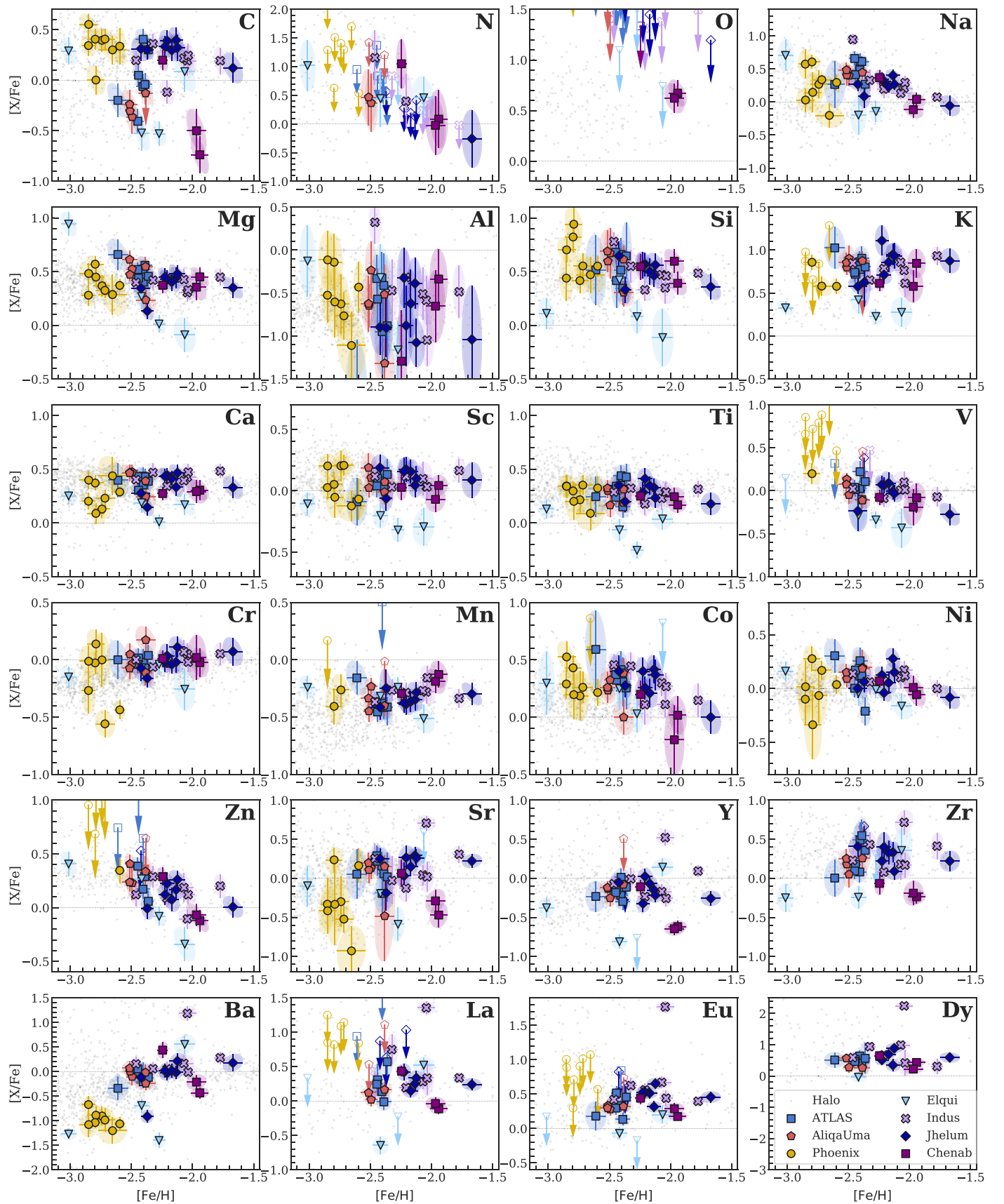


Figure 2. Element abundance ratios for all Phoenix stream stars compared to a literature compilation of Milky Way halo stars (light gray; Fulbright 2000; Barklem et al. 2005; Aoki et al. 2009; Cohen et al. 2013; Roederer et al. 2014; Abohalima & Frebel 2018), and to all other streams with high-resolution spectra acquired through the S^5 survey (Ji et al. 2020). The errors include random and systematic effects. Arrows indicate upper limits. Figure originally from Ji et al. (2020).

conclude that the intrinsic abundance spread we infer in Sr appears bona fide.

Only upper limits are available for all other neutron-capture elements. We find limits on [Eu/Fe] ranging between 0 and +1, and $\lesssim 0.82$ is our strongest limit on [La/Fe]. As the Phoenix stream stars are not clearly enhanced in r-process elements (e.g., Eu), we do not report limits on other neutron-capture elements. In particular, even among the stars with highest [Sr/Fe] abundance ratios, we do not have useful limits on other light s-process elements like Y or Zr: only one (uninformative) upper limit is available.

The remaining chemical abundance worthy of mention is the enhancement of lithium in Phoenix-10. With $A(\text{Li}) = 3.1 \pm 0.2$, Phoenix-10 easily meets the classification of a so-called lithium-rich giant star.¹⁹ The stellar parameters (and relative lifetimes of evolutionary phases) make Phoenix-10 more likely to be a core-helium-burning star than a red giant branch star, but we have no asteroseismic data to firmly distinguish these scenarios. Regardless of its evolutionary state, the observed lithium abundance exceeds what is expected for evolved stars. Figure 5 shows the lithium doublet at 6707 Å for Phoenix-10 with a best-fitting model, and the spectrum of Phoenix-3, a giant star of nearly identical temperature and no detectable lithium absorption. Phoenix-10 shows no other peculiar chemical abundances compared to other Phoenix stream stars, typical for lithium-rich giants (Casey et al. 2016).

5. Discussion

The low intrinsic scatter in metallicity we find in the Phoenix stream is consistent with the low intrinsic velocity spread, and the narrow stream width. These results imply that the former Phoenix star cluster was a low-mass ($M \sim 3 \times 10^4 M_\odot$) metal-poor globular cluster, in agreement with the previous low-resolution analysis (Wan et al. 2020). The low intrinsic scatter in metallicity strongly disfavors an ultra faint dwarf galaxy classification, where spreads of 0.2–0.3 dex are common.

The Phoenix stream has a comparable orbital energy and azimuthal action to the Palomar 5 stream, the metal-poor globular cluster NGC 5053, and the Helmi stream (Wan et al. 2020). Despite these orbital similarities, there appears to be no definitive connection in chemical abundances. The mean metallicity of Palomar 5 is $[\text{Fe}/\text{H}] = -1.48 \pm 0.10$ (Kuzma et al. 2015), distinct from Phoenix at $[\text{Fe}/\text{H}] \approx -2.7$. NGC 5053 is closer in overall metallicity (-2.30 ; Carretta et al. 2009), but still significantly different by 0.4 dex. The Helmi stream also appears unrelated, as it demonstrates a very wide spread in metallicities (-2.3 to -1.0 , Koppelman et al. 2019), that is indicative of a dwarf galaxy origin. We note that the Phoenix stream is also spatially aligned with the Hermus stream, and while there is limited abundance information for the Hermus stream, the orbits of the two streams appear inconsistent with each other (Martin et al. 2018).

We find the Phoenix stream chemical abundances are consistent with a globular cluster classification. All globular clusters show an anticorrelation between Na and O abundance ratios that is dominated by large spreads in [Na/Fe] with a depletion of [O/Fe] at the highest [Na/Fe] levels (e.g.,

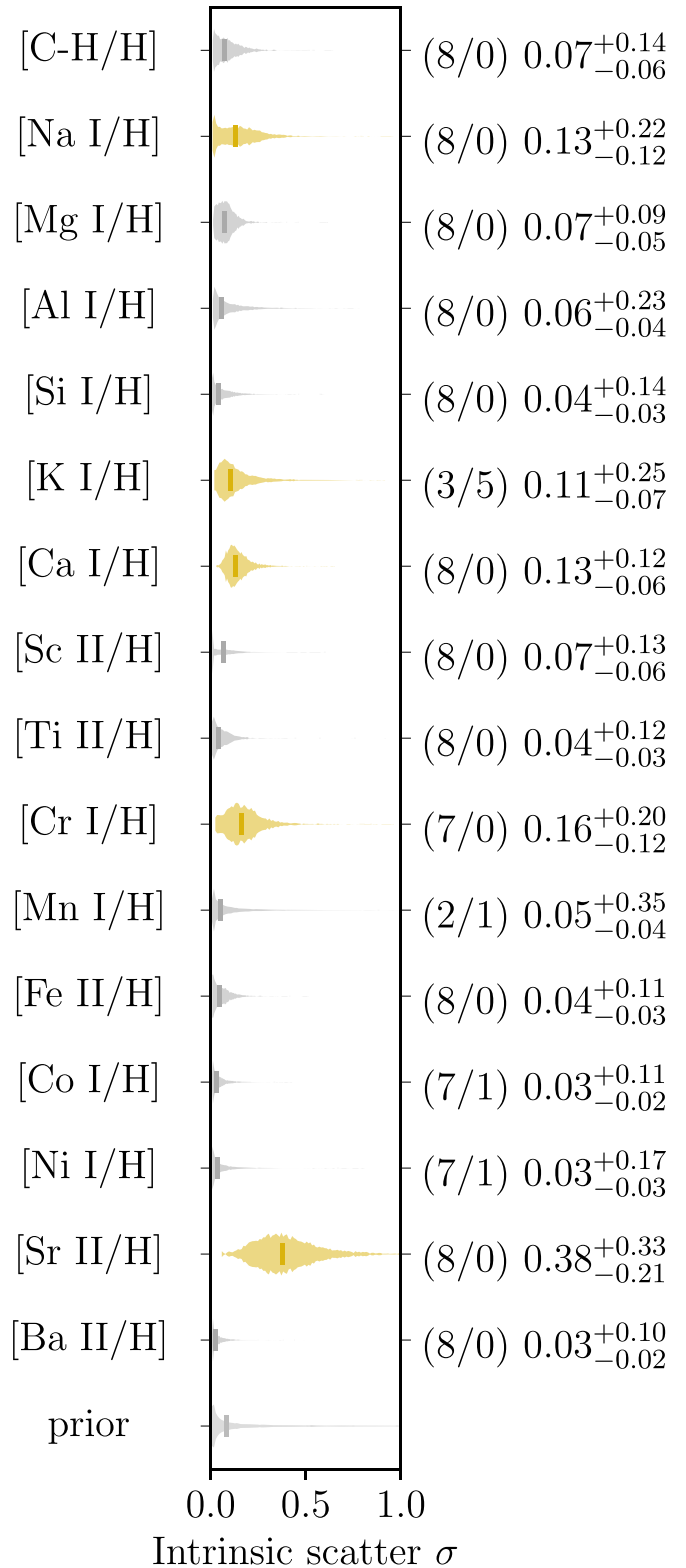


Figure 3. Intrinsic scatter in elemental abundances for the Phoenix stream. Each violin plot illustrates the posterior distribution of intrinsic scatter for that chemical element. The vertical line indicates the median value. On the right-hand side we show the (number of measurements/number of upper limits) next to the maximum a posteriori (MAP) values, as well as the 5th and 95th percentiles. For elements with only few measurements (e.g., Mn) we recover the prior (also shown) of $\log \sigma \sim \mathcal{U}(-5, 0)$. Elements shaded yellow are those with a MAP intrinsic scatter value more than 0.10 dex.

¹⁹ $A(\text{Li}) > 1.5$ is a common definition.

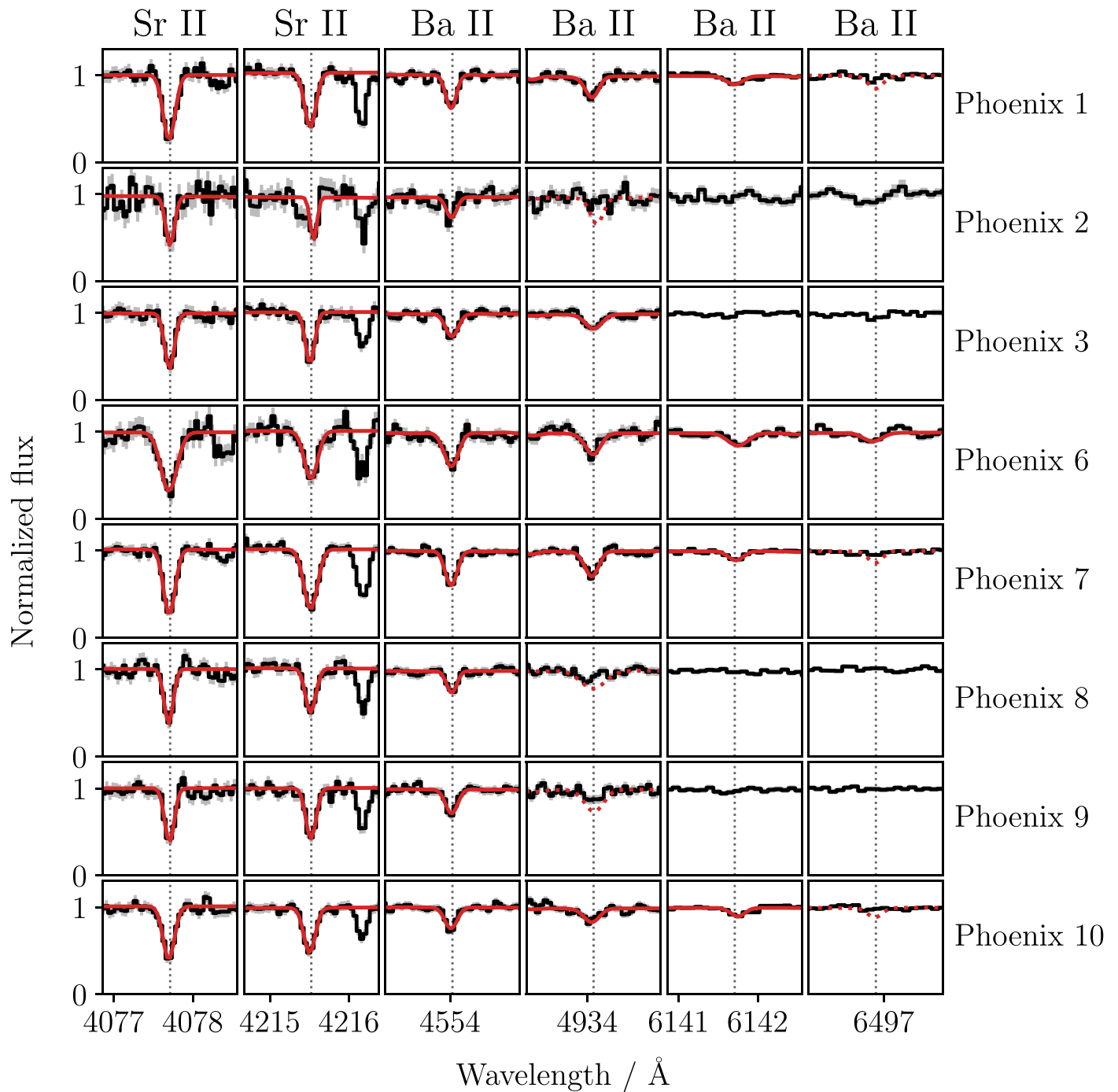


Figure 4. Continuum-normalized spectra surrounding Sr II and Ba II transitions in Phoenix stars (black). Spectral fits shown in solid red indicate measurements, and dashed red lines indicate the model was used as an upper limit. Upper limits on individual line abundances are only used if no measurements were available, which is not the case here, but for completeness we have included these upper limits that we used to ensure abundances were consistent given the line list and stellar parameters. Stars Phoenix-1 and -7 have the highest [Sr II/Fe] ratios, while Phoenix-2 has the lowest (see Table 3).

Carretta 2019). We find $[\text{Na}/\text{Fe}]^{20}$ in the Phoenix stream ranges from -0.20 to $+0.61$, nearly spanning the full range observed in globular clusters (Figure 6). Unfortunately, we only have upper limits on $[\text{O}/\text{Fe}]$ from the 630 nm absorption line, which are largely uninformative: they prevent us from detecting the presence (or absence) of any Na–O abundance correlation, despite the spread in $[\text{Na}/\text{Fe}]$.

²⁰ In this work $[\text{X}/\text{Fe}]$ and $[\text{X}/\text{H}]$ are interchangeable given the low intrinsic scatter in $[\text{Fe}/\text{H}]$.

The Mg–Al abundance pattern in globular clusters can be similarly described as a large abundance spread in $[\text{Al}/\text{Fe}]$ and a small spread in $[\text{Mg}/\text{Fe}]$, with decreasing $[\text{Mg}/\text{Fe}]$ ratios at the highest $[\text{Al}/\text{Fe}]$ ratios. While the Na–O pattern appears to be present in every globular cluster, the Mg–Al abundance pattern is either less apparent or nonexistent in lower-mass or high-metallicity globular clusters (Pancino 2018; Nataf et al. 2019). For this reason, we may not expect to see any Mg–Al relationship in a low-mass system like Phoenix, even if it were a bound globular cluster. However, globular clusters with

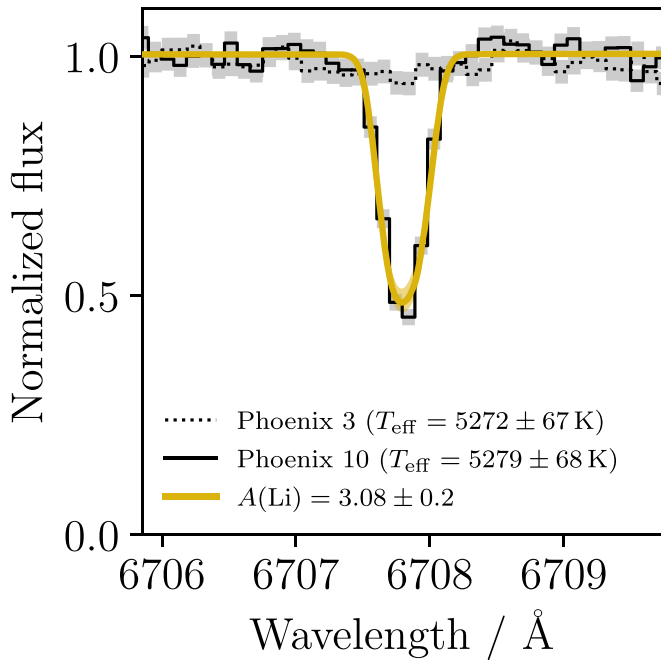


Figure 5. High-resolution spectrum of Phoenix-10 (the lithium-rich giant, with yellow showing the best-fitting model; $A(\text{Li}) = 3.1 \pm 0.2$ dex) centered at the lithium doublet at 6707 \AA compared to Phoenix-3, a lithium-normal star of comparable temperature.

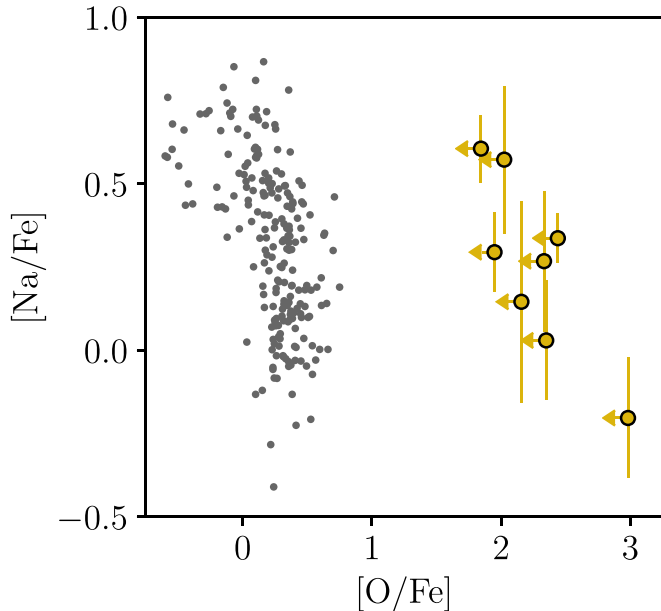


Figure 6. $[\text{O}/\text{Fe}]$ and $[\text{Na}/\text{Fe}]$ abundances for globular clusters (dark gray; Carretta et al. 2009) compared to the Phoenix stream (yellow).

strong Al enrichment also demonstrate a correlation between $[\text{Na}/\text{Fe}]$ and $[\text{Al}/\text{Fe}]$ abundances.

We find a comparable correlation in the Phoenix stream abundances. In Figure 7, we show these abundance ratios compared to Milky Way halo stars and globular cluster stars reported in the literature. This comparison warrants some discussion. We estimate $[\text{Al}/\text{H}]$ abundance ratios from the 3944 \AA and the 3961 \AA AlI absorption lines because these features are strong even in very metal-poor stars. However, most literature studies of globular clusters derive Al

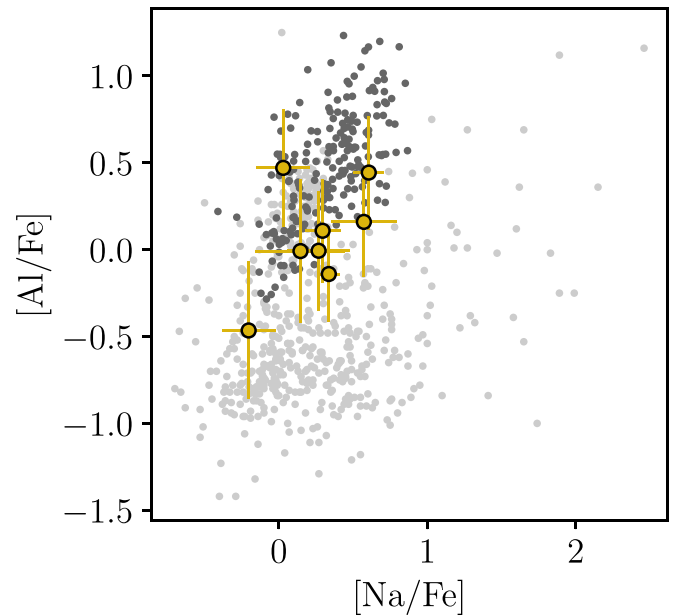


Figure 7. $[\text{Na}/\text{Fe}]$ and $[\text{Al}/\text{Fe}]$ abundances for the Phoenix stream stars (yellow) compared to literature globular cluster measurements (dark gray; Carretta et al. 2009) and Milky Way halo stars (light gray; Fulbright 2000; Barklem et al. 2005; Aoki et al. 2009; Cohen et al. 2013; Roederer et al. 2014; Abohalima & Frebel 2018). Note that the $[\text{Al}/\text{Fe}]$ abundance ratios shown here for the Phoenix stream have had non-LTE corrections applied on a per-line basis (Nordlander & Lind 2017) to be consistent with the literature values (see Section 5).

abundances from the $6696\text{--}6698 \text{ \AA}$ doublet, including those literature abundances shown in Figure 7. The $6696\text{--}6698 \text{ \AA}$ doublet would be preferable to use as is not strongly affected by non-LTE effects, but it is not visible in our spectra due to these lines being generally weaker, and because of the low S/N ratio of our spectra. Instead we are forced to use the 3944 and 3961 \AA absorption lines, but these lines *are* strongly affected by non-LTE in very metal-poor stars (Nordlander & Lind 2017). For this reason, it is prudent to apply a non-LTE correction to our $[\text{Al}/\text{Fe}]$ abundances. By accounting for the corrections on each line individually, in each star the total correction to the abundance varies between $+0.54$ and $+0.69$ dex. The corrected $[\text{Al}/\text{Fe}]$ abundances in the Phoenix stream are consistent with literature studies of globular clusters, and the $[\text{Al}/\text{Fe}]$ abundance ratios are correlated with $[\text{Na}/\text{Fe}]$ abundances,²¹ as seen in other globular clusters.

The neutron-capture elements we measure in the Phoenix stream set it distinctly apart from typical Milky Way halo stars. In Figure 2 we can see that the Phoenix stream has a very small range of $[\text{Fe}/\text{H}]$ and $[\text{Ba}/\text{Fe}]$ abundance ratios compared to other streams. ATLAS and Aliqa Uma are also concentrated in this plane and are only slightly more metal-rich than Phoenix, but their abundance ratios are more typical of what is observed in the Milky Way halo. Indeed, Aliqa Uma and ATLAS have a mean $[\text{Sr}, \text{Ba}/\text{Fe}] \sim 0$ and a small spread in both $[\text{Sr}/\text{Fe}]$ and $[\text{Ba}/\text{Fe}]$ abundance ratios. Comparing this with the Phoenix stream we find a low $[\text{Ba}/\text{Fe}] \sim -1$, coupled with a very small spread in metallicity, and large range in $[\text{Sr}/\text{Fe}]$ abundance ratios. The $[\text{Ba}/\text{Fe}]$ ratio for the Phoenix stars is a bit low compared to the field halo at the same metallicity, and low

²¹ These abundance ratios remain correlated even without the non-LTE corrections applied.

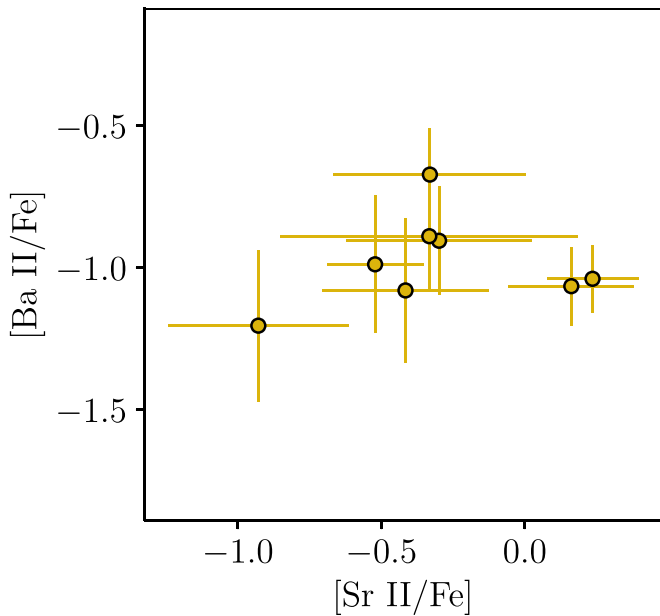


Figure 8. [Ba/Fe] and [Sr/Fe] abundance ratios for Phoenix stream stars, shown with equal-axis limits.

compared to metal-poor globular clusters, where [Ba/Fe] is typically ≈ -0.1 . This highlights the differences in Phoenix compared to other stellar streams, in a way that has not been easily possible before due to systematic differences in how chemical abundances are estimated between studies.

We find that strontium shows the largest intrinsic scatter among all elements: $\sigma([\text{Sr II}/\text{H}]) = 0.38^{+0.33}_{-0.21}$ dex (see also Figure 8). Our model for intrinsic scatter includes estimated random and dominant systematic uncertainties in abundance measurements, making it unlikely that the Sr abundance spread is a result of underestimated uncertainties in individual measurements. There are globular clusters known to show ranges in chemical elements like Sr, but these abundances are generally associated with ranges in overall metallicity (e.g., Fe-rich stars tend to be Sr-rich), and other neutron-capture elements like Ba (e.g., Marino et al. 2011; Yong et al. 2009, 2014; Sobeck et al. 2011). To our knowledge, there is no globular cluster that shows a large intrinsic spread in Sr, without an accompanying spread in overall metallicity or other neutron-capture elements.

Despite the rarity of metal-poor stars with high [Sr/Fe] and low [Ba/Fe] abundance ratios, the abundance signature is clearly not restricted to the Phoenix stream. ROA 276 is a metal-poor star ([Fe/H] ≈ -1.3) in the globular cluster ω -Centauri that has an unusually high [Sr/Ba] abundance ratio (Stanford et al. 2010), with high [X/Fe] ratios for all elements from Cu to Mo, and normal ratios for Ba to Pb (Yong et al. 2017). The best explanation for those abundance ratios was found to be enrichment from a metal-poor ([Fe/H] = -1.8) fast-rotating massive-star model of $20 M_{\odot}$, with no other nucleosynthetic source able to match the observed neutron-capture abundances. Similarly, Jacobson et al. (2015) reported on SMSS J022423-573705, an extremely metal-poor ([Fe/H] = -3.97) star with [Sr/Fe] ~ 1 and a very constraining limit of [Ba/Fe] < 0.91 .

At low metallicities strontium is produced by both the slow-neutron-capture process (s-process) and the rapid-neutron-capture process (r-process). The net products of the s-process

do not appear to be high at low metallicities for three reasons. First, at low metallicity the primary neutron source for the s-process is through the $^{22}\text{Ne}(\alpha, n)^{25}\text{Mg}$ reaction, and the rate of this reaction decreases at low metallicity. Second, the total number of neutron seeds (Fe) also decreases at low metallicity. Finally, the number of neutron poisons (e.g., ^{16}O) remains constant with metallicity, further decreasing the s-process production rate. These effects combine to produce a limiting metallicity ([Fe/H] ≈ -3.5) below which the *standard* s-process contribution becomes negligible (Prantzos et al. 1990). There are, however, variations of the main s-process that can occur at low metallicity.

One example is the rotationally boosted s-process, where a spread in strontium production is predicted as a natural consequence (Pignatari et al. 2008; Frischknecht et al. 2012, 2016). High initial rotation ($v_{\text{ini}}/v_{\text{crit}} = 0.4$) in $15\text{--}40 M_{\odot}$ stars can drive rotational mixing that allows for large amounts of ^{14}N to be produced in the hydrogen-burning shell (Meynet & Maeder 2002a, 2002b; Hirschi 2007). A significant amount of ^{14}N is eventually engulfed into the helium-burning core, where it is transformed into ^{22}Ne through the $^{14}\text{N}(\alpha, \gamma)^{18}\text{F}(\beta^+\nu)^{18}\text{O}(\alpha, \gamma)^{22}\text{Ne}$ reaction chain. As stated earlier, the increase in ^{22}Ne favors s-process production because the main neutron source for the s-process at low metallicity is produced through the $^{22}\text{Ne}(\alpha, n)^{25}\text{Mg}$ reaction. At this point s-process nucleosynthesis is limited only by the number of seeds (Fe nuclei) available, as the amount of neutron poisons does not change with rotation. Indeed, rotation largely only acts through the ^{22}Ne source, as changes to the size of the hydrogen- and helium-burning regions due to rotation have a relatively small effect on nucleosynthetic yields.

Rotation can increase s-process nucleosynthesis in both metal-poor and metal-rich stars, but the nucleosynthetic signature is more distinctive at lower metallicities. In massive stars the neutron source is less efficient than in low-mass asymptotic giant branch (AGB) stars, which shifts the element production to the first peak (e.g., Sr) instead of later peaks (e.g., Ba). The s-process elements produced are then lost to the interstellar medium, either during substantial mass loss in winds in the final stages of stellar evolution (e.g., Banerjee et al. 2019), or after the massive star explodes in a core-collapse supernova. Stars more massive than $40 M_{\odot}$ are not considered to contribute to s-process nucleosynthesis because they are thought to collapse directly into black holes (Woosley et al. 2002; Heger et al. 2003).

We hypothesize that the Phoenix stream Sr abundances are consistent with enrichment from a massive fast-rotating metal-poor star²² that has undergone s-process nucleosynthesis, and enriched the surrounding interstellar medium with neutron-capture elements. In this scenario, since the Phoenix star cluster was likely low mass—and not massive enough to retain ejecta—we suggest that the massive fast-rotating star existed in a previous generation of star formation, before the cluster reached [Fe/H] ≈ -2.7 . The nucleosynthetic products of that massive fast-rotating star were then likely inhomogeneously mixed into the pre-Phoenix gas cloud, which would account for the variations in Sr abundances of individual stars in the present generation. For these reasons, we only consider massive fast-rotating metal-poor star models below this metallicity.

²² Or stars, but we find a single massive fast-rotating metal-poor star provides a sufficient description for the abundances.

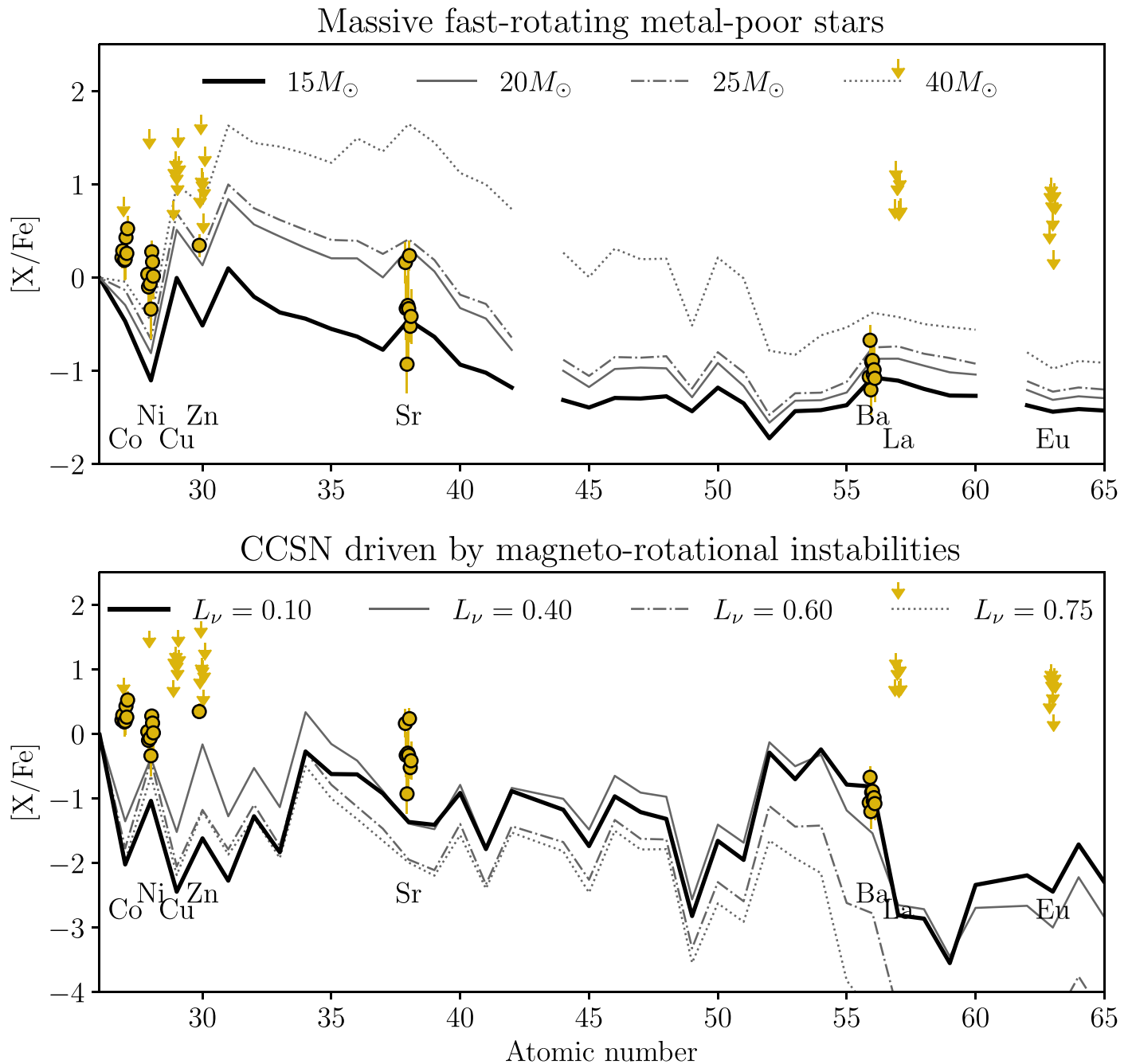


Figure 9. Predicted yields for two scenarios: massive fast-rotating metal-poor stars where neutron-capture elements are produced by rotationally driven s-process production (top; Frischknecht et al. 2012, 2016), and core-collapse supernovae that are driven by a magneto-rotational instability (Nishimura et al. 2017). The massive fast-rotating metal-poor star predictions are for $[\text{Fe}/\text{H}] = -3.8$ with a rotation speed $v_{\text{ini}}/v_{\text{crit}} = 0.4$. The lower panel shows yield predictions for models with varying magnetic-driving strengths: the $\hat{L}_\nu = 0.10$ has the strongest influence of magnetic fields, the $\hat{L}_\nu = 1$ model (not shown) is dominated by neutrino heating, and $\hat{L}_\nu \approx 0.40\text{--}0.75$ are intermediate models between the two extrema. The observed abundance ratios are normalized to $[\text{Fe}/\text{H}]$.

We compared the Phoenix stream abundances to nucleosynthetic yields for fast-rotating metal-poor ($v_{\text{ini}}/v_{\text{crit}} = 0.4$; $[\text{Fe}/\text{H}] = -3.8$) stars of $15\text{--}40 M_\odot$ (Frischknecht et al. 2016). The $v_{\text{ini}}/v_{\text{crit}}$ ratio defines the initial rotational velocity relative to the critical breakup speed. We also considered models with $[\text{Fe}/\text{H}] = -5.8$, and models that rotate up to $v_{\text{ini}}/v_{\text{crit}} = 0.6$, but found them to be unreasonable fits to the data. We note that the yields provided in Frischknecht et al. (2016) are pre-explosive yields, only up to the end of oxygen burning. We assume that the total s-process yields are not strongly modified by core-collapse supernovae (e.g., Tur et al. 2009), and restrict our comparison to

heavy elements ($Z > 26$; however, see Maeder et al. 2015; Choplin 2019). We show the expected yields in the top panel of Figure 9, assuming that $\approx 10^{-5} M_\odot$ of Fe is produced during core collapse. If we increase the amount of Fe produced to exceed $10^{-4} M_\odot$, then we find poor fits to the $[\text{Ni}/\text{Fe}]$ measurements. However, the relationship between the amount of Fe produced and the final abundance patterns primarily depend on how much of the s-process elements are deposited into the interstellar medium through stellar winds, and how much are released during core collapse. As we expand upon below, the first-order parameters that control Sr production here are the rotation rate and the stellar mass.

In these massive fast-rotating metal-poor star models the rotation rate largely governs the abundance ratios of first (Sr) to second (Ba) peak s-process elements, as long as there are sufficient seeds available. The set of models available to us only include zero or high rotation ($v_{\text{ini}}/v_{\text{crit}} = 0$ or >0.4), but we find a reasonable quantitative fit from the high rotation models. The nonrotating models (equivalent in all other parameters) do not produce any appreciable amounts of Sr or Ba, or Fe-peak elements. For this reason, we find that the nonrotating models cannot reproduce the abundance ratios we observe. It is reasonable to assume that a different initial rotation speed, for the same set of model masses and metallicities, could provide a better description for these data (Limongi & Chieffi 2018; Rizzuti et al. 2019).

The $15 M_{\odot}$ model provides the most consistent fit to the mean abundances, but we find that a $20\text{--}25 M_{\odot}$ model would also provide a reasonable explanation. All heavy elements measured (Co, Ni, Cu, Zn, Sr, Ba) contribute to placing these constraints. Similarly, with these models if we assume no additional Fe production then the models tend to overproduce $[\text{Zn}/\text{Fe}]$ (and heavier elements). While we only have one measurement of $[\text{Zn}/\text{Fe}]$ —in the star with the highest $[\text{Sr}/\text{Fe}]$ measurement—the upper limits of $[\text{Zn}/\text{Fe}]$ from other stars helps constrain the range of suitable models. All of these fast-rotating metal-poor star models are consistent with our observations in that they overproduce $[\text{Sr}/\text{Fe}]$ relative to $[\text{Ba}/\text{Fe}]$. We note that the abundance comparisons we are making here explicitly ignore any nucleosynthesis contributions that occur between the enrichment from the massive fast-rotating star and the present day.

The predicted nucleosynthetic yields from massive and fast-rotating metal-poor stars clearly provide a good description for the neutron-capture abundances we observe in the Phoenix stream. However, there is another potential issue with this scenario that is worth commenting on. An argument proposed in favor of fast rotation in metal-poor stars is that they are more compact than their metal-rich equivalents, and thus metal-poor stars should rotate faster (Frischke et al. 2016). However, evidence suggests that the stellar multiplicity fraction increases (to $\approx 100\%$) as overall metallicity decreases, and as primary mass increases, implying that nearly all massive and metal-poor stars should be in binaries (e.g., Badenes et al. 2018). In a binary system the rotation of both stars is constrained by the orbital period of the system, which can never be shorter than a few days. This sets a critical upper limit for the rotation speed of nearly all massive metal-poor stars, which is far less than the $v_{\text{ini}}/v_{\text{crit}} = 0.4$ ratios considered here. This might make fast-rotating massive and/or metal-poor stars a rare occurrence due to the increased multiplicity fraction for those kinds of systems, even though these models provide a good match to our observations.

We also considered predicted yields from metal-poor AGB stars, the dominant source of the main s-process in the present day. The main s-process can still occur in metal-poor environments, but it is less efficient for reasons described earlier. The typical yields of most low-metallicity AGB stars produce more barium relative to strontium (e.g., Fishlock et al. 2014), unlike what we see in the Phoenix stream. We compared the Phoenix stream abundances to yields from 102 metal-poor ($Z = 0.0001$) low- and intermediate-mass AGB star models (Lugaro et al. 2012; Karakas & Lattanzio 2014) and find that only very few (intermediate-mass) models can produce

significantly higher $[\text{Sr}/\text{H}]$ than $[\text{Ba}/\text{H}]$. Even among those intermediate-mass AGB models, the observed $[\text{Ba}/\text{Fe}]$ ratio is an order of magnitude smaller than those predicted by the models. While low- and intermediate-mass AGB stars would be an appealing scenario, we conclude that this is an unlikely explanation for the neutron-capture abundances in the Phoenix stream.

However, the r-process could also qualitatively reproduce the abundances in the Phoenix stream. Neutrino-driven winds produce neutron-capture elements through the r-process, with net yields that tend to favor *lighter* elements like Sr and Ba, instead of Eu (Arcones & Thielemann 2013; Wanajo 2013). Magneto-rotational instabilities during a core-collapse supernova is another example where heavy elements are produced through the r-process, but favoring elements between $Z \sim 35\text{--}55$. In the lower panel of Figure 9 we show yield predictions for core-collapse supernovae that are driven by magneto-rotational instabilities (Nishimura et al. 2017). Multiple models are shown, representing models dominated by magnetically driven jets (low \hat{L}_{ν} : $\hat{L}_{\nu} \lesssim 0.4$), or intermediate models that are driven in part by magnetic fields and neutrino heating ($\hat{L}_{\nu} \approx 0.5\text{--}0.75$). We also considered models that are purely dominated by neutrino heating ($\hat{L}_{\nu} \gtrsim 1.0$) but these models underpredicted Ba (relative to Sr) by orders of magnitude, and are not shown in Figure 9. Depending on the properties of the driving mechanism, these models can qualitatively produce a high $[\text{Sr}/\text{Ba}]$ abundance ratio, like that observed in the Phoenix stream. The magnetic-driven models (low \hat{L}_{ν}) tend to be in better agreement with the Phoenix stream abundances, and Fe-peak elements (Co, Ni, Cu, and Zn) are underpredicted by all of these models. This could conceivably be explained by additional supernovae that contribute to the interstellar medium before the Phoenix cluster formed, but overall we conclude that core-collapse supernovae that are driven by magneto-rotational instabilities tend to be a poorer explanation for the Phoenix stream observations.

One final enrichment scenario that could explain the Phoenix stream abundances is an electron-capture supernova (ECSN). These explosions occur from low-mass ($\lesssim 10 M_{\odot}$) super AGB stars that form an electron-degenerate oxygen-neon-magnesium core mass of around $\sim 1.1 M_{\odot}$. Hydrogen and helium shell burning continuously increases the core mass, forcing the core to contract. As the central density rises, electron capture onto ^{24}Mg is induced, reducing electron density and further accelerating core contraction. Eventually, electron capture on ^{20}Ne can lead to an ignition that leads to an ECSN (Nomoto & Leung 2017). This is one of the candidate sites for the r-process, which can account for much of the heavy element nucleosynthesis at low metallicities (Kobayashi et al. 2020). In particular, the galactic enrichment of Sr at low metallicities $[\text{Fe}/\text{H}] \approx -3.8$ can be entirely explained by ECSN, without the need for a lighter elements primary process (Cristallo et al. 2015; Kobayashi et al. 2020). Detailed simulations of 8.8 and 9.6 M_{\odot} progenitors show that Sr, Zr, and Zn are overproduced during ECSN (Wanajo et al. 2018), with small amounts of Ni and Cu, and negligible quantities of Ba and Eu produced. This qualitatively matches the abundance pattern observed in the Phoenix stream, if we assume that the products of an ECSN are inhomogeneously mixed into the pre-Phoenix gas cloud, just like the massive fast-rotating metal-poor star scenario. The occurrence of ECSN is not well known—the fraction of CCSN that are ignited by electron capture varies between $f_{\text{ECSN}} = 0.01$

and 0.3 (Wanajo et al. 2009)—but ECSN are at least frequent enough to account for the galactic enrichment of Sr at low metallicity (Kobayashi et al. 2020). For these reasons, a single²³ ECSN is a plausible alternative for the neutron-capture abundances in the Phoenix stream. Unfortunately, given the limited abundance measurements and the lack of published ECSN yields, it is difficult to further constrain this scenario.

We do not consider neutron star mergers here, or neutrino winds during those mergers. There are considerations that the delay-time distribution of coalescence times may make neutron star mergers an unlikely contributor in very low-metallicity environments (e.g., Côté et al. 2019). It is also generally considered that neutron star mergers produce large amounts of heavy r-process elements, including Ba, and would not satisfy the low Ba scatter constraint. However, there is evidence that the kilonova associated with the GW 170817 event appears to have produced a very high Sr/Eu ratio, about 10 times higher than the solar r-process pattern (Ji et al. 2019). If later observations and nucleosynthesis calculations demonstrate that neutron star merger yields are dominated by light r-process elements like Sr, then this may represent a plausible explanation for the Sr scatter in the Phoenix stream. But we consider this scenario unlikely given current models and observations.

5.1. Phoenix-10, the Lithium-rich Giant Star

Phoenix-10 shows an overabundance of lithium for a typical giant star, which is likely unrelated to the other chemical abundance patterns in the stream. Lithium is a fragile element that is difficult to produce in net quantities in standard single star evolution (e.g., Iben 1967). In most stars the surface lithium abundance decreases as they evolve off the main sequence and experience first dredge up, where surface layers are mixed into deeper, hotter regions. As a consequence, most giant stars have very little lithium at their surface, as is the case for the other Phoenix stars. However, it is also known that about $\sim 1\%$ of red giants are classified as lithium-rich, $A(\text{Li}) > 1.5$ dex. The incidence of lithium-rich giants increases with overall metallicity from $\approx 0.5\%$ at $[\text{Fe}/\text{H}] = -2$ to $\approx 1.5\%$ at $[\text{Fe}/\text{H}] = +0.5$ (Casey et al. 2019). At $[\text{Fe}/\text{H}] \sim -2.9$, Phoenix-10 is among the most metal-poor lithium-rich giants known (Casey et al. 2016).

Lithium-rich giants have been discovered in the Milky Way disk, halo, and in open and globular star clusters. Most are discovered serendipitously (for a literature compendium see Casey et al. 2016), and currently about 4000 lithium-rich giants are known (Casey et al. 2019; Gao et al. 2019). While many mechanisms have been proposed to explain lithium-rich giants, one that remains consistent with the observations across the entire giant branch is where tidal interactions in a binary system drive sufficient mixing to produce lithium internally and bring it up to the surface (Casey et al. 2019). This would allow for lithium enrichment at any point along the red giant branch, and would naturally explain the high frequency ($80_{-6}^{+7}\%$) of lithium-rich giants that have helium-burning cores (Casey et al. 2019). We have two epochs of radial velocity measurements for Phoenix-10, separated by about 1 month. The radial velocity difference between epochs is $\approx 1 \text{ km s}^{-1}$ and within the joint uncertainties. If the enhanced lithium in Phoenix-10 were due to tidal interactions in a binary system, then the expected radial

velocity variation could be much smaller than our radial velocity precision ($\approx 1 \text{ km s}^{-1}$), as a large range of orbital periods and mass ratios are capable of driving sufficient tidal interactions.

6. Conclusions

We confirm that the Phoenix stream is consistent with being a disrupted globular cluster. From high-resolution spectra we find the mean metallicity is $[\text{Fe II}/\text{H}] = -2.71 \pm 0.07$ and the low intrinsic metallicity spread ($\sigma([\text{Fe II}/\text{H}]) = 0.04_{-0.03}^{+0.11}$), is consistent with zero. The large peak-to-peak range of abundance ratios in $[\text{Al}/\text{Fe}]$ and $[\text{Na}/\text{Fe}]$ are consistent with metal-poor globular clusters.

The neutron-capture abundance ratios in the Phoenix stream are not seen in any other globular cluster. Low $[\text{Ba}/\text{Fe}]$ abundance ratios, with no measurable spread in $[\text{Ba}/\text{Fe}]$ across the stream, are accompanied by a large intrinsic scatter in $[\text{Sr}/\text{Fe}]$. We find that the rotationally boosted s-process from a massive fast-rotating metal-poor star ($15 M_{\odot}$, $v_{\text{ini}}/v_{\text{crit}} = 0.4$, $[\text{Fe}/\text{H}] = -3.8$) provides the best explanation for these abundances. Since the Phoenix progenitor system was likely low mass, it suggests that this fast-rotating metal-poor star enriched the interstellar medium at very high redshift, before the cluster formed.

While the Phoenix progenitor system would be the most metal-poor globular cluster known, there is every likelihood that many comparable systems existed and have since disrupted (Larsen et al. 2012; Beasley et al. 2019; Krumholz et al. 2019). The relative isolation of Phoenix in the Galactic halo, with an orbital inclination of 60° relative to the disk, and a pericenter of 13 kpc (Wan et al. 2020), has helped prevent the Phoenix stars becoming well mixed with the bulk of the Milky Way stellar population and left them detectable as a stellar stream.

We have shown how the detailed abundances of ancient metal-poor stars can provide unique insight into nucleosynthesis events in the very early universe. Ultra faint dwarf galaxies, globular clusters, and ancient metal-poor stars in the Milky Way halo all offer the prospect for uncovering stars with unusual chemical abundance signatures (see discussion in Karlsson et al. 2013). However, the Phoenix stream represents an example of a potentially rich source for ancient stars with peculiar chemical abundances: identifying disrupted systems in phase space can reveal chemical records of nucleosynthesis events. These relics are rare, but each of them contribute to our knowledge of the very early universe.

We thank the anonymous referee for a timely and fastidious report, which improved this paper. We thank Amanda Karakas (Monash) for providing yields of metal-poor low- and intermediate-mass AGB stars, David Yong (ANU) for help in interpreting the yield comparisons with ROA 276, and Kevin Schlaufman (JHU) for productive conversations. This paper includes data gathered with the 6.5 m Magellan Telescopes located at Las Campanas Observatory, Chile. A.R.C. is supported in part by the Australian Research Council through a Discovery Early Career Researcher Award (DE190100656). Parts of this research were supported by the Australian Research Council Centre of Excellence for All Sky Astrophysics in 3 Dimensions (ASTRO 3D), through project number CE170100013.

T.S.L. is supported by NASA through Hubble Fellowship grant HF2-51439.001 awarded by the Space Telescope Science

²³ Or many.

Institute, which is operated by the Association of Universities for Research in Astronomy, Inc., for NASA, under contract NAS5-26555. T.S.L., A.P.J., and Y.Y.M. are supported by NASA through Hubble Fellowship grants HST-HF2-51439.001, HST-HF2-51393.001, and HST-HF2-51441.001, respectively, awarded by the Space Telescope Science Institute, which is operated by the Association of Universities for Research in Astronomy, Inc., for NASA, under contract NAS5-26555. S.K. was partially supported by NSF grant AST-1813881 and Heising-Simons foundation grant 2018-1030. J.D. Simpson, S.L.M., and D.B.Z. acknowledge the support of the Australian Research Council (ARC) through Discovery Project grant DP180101791. G.S.D-C. also acknowledges ARC support through Discovery Project grant DP150103294. J.D.S. was supported in part by the National Science Foundation through grant AST-1714873. A.B.P. is supported by NSF grant AST-1813881.

This research has made use of the SIMBAD database, operated at CDS, Strasbourg, France (Wenger et al. 2000), and NASA’s Astrophysics Data System Bibliographic Services.

This work presents results from the European Space Agency (ESA) space mission Gaia. Gaia data are being processed by the Gaia Data Processing and Analysis Consortium (DPAC). Funding for the DPAC is provided by national institutions, in particular the institutions participating in the Gaia MultiLateral Agreement (MLA). The Gaia mission website is <https://www.cosmos.esa.int/gaia>. The Gaia archive website is <https://archives.esac.esa.int/gaia>.

This project used public archival data from the Dark Energy Survey (DES). Funding for the DES Projects has been provided by the U.S. Department of Energy, the U.S. National Science Foundation, the Ministry of Science and Education of Spain, the Science and Technology Facilities Council of the United Kingdom, the Higher Education Funding Council for England, the National Center for Supercomputing Applications at the University of Illinois at Urbana-Champaign, the Kavli Institute of Cosmological Physics at the University of Chicago, the Center for Cosmology and Astro-Particle Physics at the Ohio State University, the Mitchell Institute for Fundamental Physics and Astronomy at Texas A&M University, Financiadora de Estudos e Projetos, Fundação Carlos Chagas Filho de Amparo à Pesquisa do Estado do Rio de Janeiro, Conselho Nacional de Desenvolvimento Científico e Tecnológico and the Ministério da Ciência, Tecnologia e Inovação, the Deutsche Forschungsgemeinschaft, and the Collaborating Institutions in the Dark Energy Survey. The Collaborating Institutions are Argonne National Laboratory, the University of California at Santa Cruz, the University of Cambridge, Centro de Investigaciones Energéticas, Medioambientales y Tecnológicas-Madrid, the University of Chicago, University College London, the DES-Brazil Consortium, the University of Edinburgh, the Eidgenössische Technische Hochschule (ETH) Zürich, Fermi National Accelerator Laboratory, the University of Illinois at Urbana-Champaign, the Institut de Ciències de l’Espai (IEEC/CSIC), the Institut de Física d’Altes Energies, Lawrence Berkeley National Laboratory, the Ludwig-Maximilians Universität München and the associated Excellence Cluster Universe, the University of Michigan, the National Optical Astronomy Observatory, the University of Nottingham, The Ohio State University, the OzDES Membership Consortium, the University of Pennsylvania, the University of Portsmouth, SLAC National Accelerator Laboratory, Stanford University, the

University of Sussex, and Texas A&M University. Based in part on observations at Cerro Tololo Inter-American Observatory, National Optical Astronomy Observatory, which is operated by the Association of Universities for Research in Astronomy (AURA) under a cooperative agreement with the National Science Foundation.

The Legacy Surveys consist of three individual and complementary projects: the Dark Energy Camera Legacy Survey (DECaLS; NOAO Proposal ID # 2014B-0404; PIs: David Schlegel and Arjun Dey), the Beijing-Arizona Sky Survey (BASS; NOAO Proposal ID # 2015A-0801; PIs: Zhou Xu and Xiaohui Fan), and the Mayall *z*-band Legacy Survey (MzLS; NOAO Proposal ID # 2016A-0453; PI: Arjun Dey). DECaLS, BASS and MzLS together include data obtained, respectively, at the Blanco telescope, Cerro Tololo Inter-American Observatory, National Optical Astronomy Observatory (NOAO); the Bok telescope, Steward Observatory, University of Arizona; and the Mayall telescope, Kitt Peak National Observatory, NOAO. The Legacy Surveys project is honored to be permitted to conduct astronomical research on Iolkam Du’ag (Kitt Peak), a mountain with particular significance to the Tohono O’odham Nation.

NOAO is operated by the Association of Universities for Research in Astronomy (AURA) under a cooperative agreement with the National Science Foundation.

The Legacy Survey team makes use of data products from the Near-Earth Object Wide-field Infrared Survey Explorer (NEOWISE), which is a project of the Jet Propulsion Laboratory/California Institute of Technology. NEOWISE is funded by the National Aeronautics and Space Administration.

The Legacy Surveys imaging of the DESI footprint is supported by the Director, Office of Science, Office of High Energy Physics of the U.S. Department of Energy under Contract No. DE-AC02-05CH1123, by the National Energy Research Scientific Computing Center, a DOE Office of Science User Facility under the same contract; and by the U.S. National Science Foundation, Division of Astronomical Sciences under Contract No. AST-0950945 to NOAO.







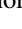









The Pan-STARRS1 Surveys (PS1) and the PS1 public science archive have been made possible through contributions by the Institute for Astronomy, the University of Hawaii, the Pan-STARRS Project Office, the Max Planck Society and its participating institutes, the Max Planck Institute for Astronomy, Heidelberg and the Max Planck Institute for Extraterrestrial Physics, Garching, The Johns Hopkins University, Durham University, the University of Edinburgh, the Queen’s University Belfast, the Harvard-Smithsonian Center for Astrophysics, the Las Cumbres Observatory Global Telescope Network Incorporated, the National Central University of Taiwan, the Space Telescope Science Institute, the National Aeronautics and Space Administration under grant No. NNX08AR22G issued through the Planetary Science Division of the NASA Science Mission Directorate, the National Science Foundation grant No. AST-1238877, the University of Maryland, Eotvos Lorand University (ELTE), the Los Alamos National Laboratory, and the Gordon and Betty Moore Foundation.

This manuscript has been authored by Fermi Research Alliance, LLC under Contract No. DE-AC02-07CH11359 with the U.S. Department of Energy, Office of Science, Office of High Energy Physics. The United States Government retains and the publisher, by accepting the article for publication,

acknowledges that the United States Government retains a nonexclusive, paid-up, irrevocable, worldwide license to publish or reproduce the published form of this manuscript, or allow others to do so, for United States Government purposes.

Software: Stan (Salvatier et al. 2016; Carpenter et al. 2017), ATLAS (Castelli & Kurucz 2003), MOOG (Snedden 1973; Sobeck et al. 2011), SMHR (Casey 2014).

ORCID iDs

Andrew R. Casey  <https://orcid.org/0000-0003-0174-0564>
 Alexander P. Ji  <https://orcid.org/0000-0002-4863-8842>
 Terese T. Hansen  <https://orcid.org/0000-0001-6154-8983>
 Ting S. Li  <https://orcid.org/0000-0002-9110-6163>
 Sergey E. Kuposov  <https://orcid.org/0000-0003-2644-135X>
 Gary S. Da Costa  <https://orcid.org/0000-0001-7019-649X>
 Joss Bland-Hawthorn  <https://orcid.org/0000-0001-7516-4016>
 Lara Cullinane  <https://orcid.org/0000-0001-8536-0547>
 Denis Erkal  <https://orcid.org/0000-0002-8448-5505>
 Geraint F. Lewis  <https://orcid.org/0000-0003-3081-9319>
 Kyler Kuehn  <https://orcid.org/0000-0003-0120-0808>
 Dougal Mackey  <https://orcid.org/0000-0002-6529-8093>
 Sarah L. Martell  <https://orcid.org/0000-0002-3430-4163>
 Andrew B. Pace  <https://orcid.org/0000-0002-6021-8760>
 Jeffrey D. Simpson  <https://orcid.org/0000-0002-8165-2507>
 Daniel B. Zucker  <https://orcid.org/0000-0003-1124-8477>

References

- Abomalima, A., & Frebel, A. 2018, *ApJS*, 238, 36
 Andrievsky, S. M., Spite, F., Korotin, S. A., et al. 2011, *A&A*, 530, A105
 Aoki, W., Arimoto, N., Sadakane, K., et al. 2009, *A&A*, 502, 569
 Arcones, A., & Thielemann, F. K. 2013, *JPhG*, 40, 013201
 Badenes, C., Mazzola, C., Thompson, T. A., et al. 2018, *ApJ*, 854, 147
 Balbinot, E., Yanny, B., Li, T. S., et al. 2016, *ApJ*, 820, 58
 Banerjee, P., Heger, A., & Qian, Y.-Z. 2019, *ApJ*, 887, 187
 Barklem, P. S., Christlieb, N., Beers, T. C., et al. 2005, *A&A*, 439, 129
 Beasley, M. A., Leaman, R., Gallart, C., et al. 2019, *MNRAS*, 487, 1986
 Belokurov, V., Zucker, D. B., Evans, N. W., et al. 2007, *ApJ*, 654, 897
 Bernstein, R., Shectman, S. A., Gunnels, S. M., Mochnacki, S., & Athey, A. E. 2003, *Proc. SPIE*, 4841, 1694
 Bonaca, A., Geha, M., & Kallivayalil, N. 2012, *ApJL*, 760, L6
 Carpenter, B., Gelman, A., Hoffman, M. D., et al. 2017, *J. Stat. Softw.*, 76, 1
 Carrera, R., Pancino, E., Gallart, C., & del Pino, A. 2013, *MNRAS*, 434, 1681
 Carretta, E. 2019, *A&A*, 624, A24
 Carretta, E., Bragaglia, A., Gratton, R. G., et al. 2009, *A&A*, 505, 117
 Casagrande, L., & Vandenberg, D. A. 2014, *MNRAS*, 444, 392
 Casey, A. R. 2014, PhD thesis, Australian National Univ.
 Casey, A. R., Ho, A. Y. Q., Ness, M., et al. 2019, *ApJ*, 880, 125
 Casey, A. R., Ruchti, G., Masseron, T., et al. 2016, *MNRAS*, 461, 3336
 Castelli, F., & Kurucz, R. L. 2003, in IAU Symp. 210, Modeling of Stellar Atmospheres, ed. N. Piskunov, W. W. Weiss, & D. F. Gray (Cambridge: Cambridge Univ. Press), A20
 Choplin, A. 2019, arXiv:1901.10708
 Cohen, J. G., Christlieb, N., Thompson, I., et al. 2013, *ApJ*, 778, 56
 Côté, B., Eichler, M., Arcones, A., et al. 2019, *ApJ*, 875, 106
 Cristallo, S., Abia, C., Straniero, O., & Piersanti, L. 2015, *ApJ*, 801, 53
 DES Collaboration, Abbott, T. M. C., Abdalla, F. B., et al. 2018, *ApJS*, 239, 18
 Dotter, A., Chaboyer, B., Jevremović, D., et al. 2008, *ApJS*, 178, 89
 Erkal, D., Sanders, J. L., & Belokurov, V. 2016, *MNRAS*, 461, 1590
 Fishlock, C. K., Karakas, A. I., Lugaro, M., & Yong, D. 2014, *ApJ*, 797, 44
 Frebel, A., Simon, J. D., Geha, M., & Willman, B. 2010, *ApJ*, 708, 560
 Frischknecht, U., Hirschi, R., Pignatari, M., et al. 2016, *MNRAS*, 456, 1803
 Frischknecht, U., Hirschi, R., & Thielemann, F. K. 2012, *A&A*, 538, L2
 Fulbright, J. P. 2000, *AJ*, 120, 1841
 Gaia Collaboration, Brown, A. G. A., Vallenari, A., et al. 2018, *A&A*, 616, A1
 Gao, Q., Shi, J.-R., Yan, H.-L., et al. 2019, *ApJS*, 245, 33
 Hansen, C. J., Bergemann, M., Cescutti, G., et al. 2013, *A&A*, 551, A57
 Heger, A., Fryer, C. L., Woosley, S. E., Langer, N., & Hartmann, D. H. 2003, *ApJ*, 591, 288
 Hirschi, R. 2007, *A&A*, 461, 571
 Ibata, R. A., Gilmore, G., & Irwin, M. J. 1994, *Natur*, 370, 194
 Iben, I. J. 1967, *ApJ*, 147, 624
 Jacobson, H. R., Keller, S., Frebel, A., et al. 2015, *ApJ*, 807, 171
 Ji, A. P., Li, T. S., Hansen, T. T., et al. 2020, *AJ*, 160, 181
 Ji, A. P., Simon, J. D., Frebel, A., Venn, K. A., & Hansen, T. T. 2019, *ApJ*, 870, 83
 Karakas, A. I., & Lattanzio, J. C. 2014, *PASA*, 31, e030
 Karlsson, T., Bromm, V., & Bland-Hawthorn, J. 2013, *RvMP*, 85, 809
 Kelson, D. D. 2003, *PASP*, 115, 688
 Kobayashi, C., Karakas, A. I., & Lugaro, M. 2020, *ApJ*, 900, 179
 Koppelman, H. H., Helmi, A., Massari, D., Roelenga, S., & Bastian, U. 2019, *A&A*, 625, A5
 Krumholz, M. R., McKee, C. F., & Bland-Hawthorn, J. 2019, *ARA&A*, 57, 227
 Kuzma, P. B., Da Costa, G. S., Keller, S. C., & Maunder, E. 2015, *MNRAS*, 446, 3297
 Larsen, S. S., Brodie, J. P., & Strader, J. 2012, *A&A*, 546, A53
 Li, T. S., Kuposov, S. E., Zucker, D. B., et al. 2019, *MNRAS*, 490, 3508
 Limongi, M., & Chieffi, A. 2018, *ApJS*, 237, 13
 Lugaro, M., Karakas, A. I., Stancliffe, R. J., & Rijs, C. 2012, *ApJ*, 747, 2
 Maeder, A., Meynet, G., & Chiappini, C. 2015, *A&A*, 576, A56
 Marino, A. F., Milone, A. P., Piotto, G., et al. 2011, *ApJ*, 731, 64
 Martin, C., Amy, P. M., Newberg, H. J., et al. 2018, *MNRAS*, 477, 2419
 Meynet, G., & Maeder, A. 2002a, *A&A*, 390, 561
 Meynet, G., & Maeder, A. 2002b, *A&A*, 381, L25
 Morganson, E., Gruendl, R. A., Menanteau, F., et al. 2018, *PASP*, 130, 074501
 Nataf, D. M., Wyse, R. F. G., Schiavon, R. P., et al. 2019, *AJ*, 158, 14
 Nishimura, N., Sawai, H., Takiwaki, T., Yamada, S., & Thielemann, F. K. 2017, *ApJL*, 836, L21
 Nomoto, K., & Leung, S.-C. 2017, in Handbook of Supernovae, ed. A. W. Alsabti & P. Murdin (Cham: Springer International Publishing), 483
 Nordlander, T., & Lind, K. 2017, *A&A*, 607, A75
 Pancino, E. 2018, *A&A*, 614, A80
 Pignatari, M., Gallino, R., Meynet, G., et al. 2008, *ApJL*, 687, L95
 Prantzos, N., Hashimoto, M., & Nomoto, K. 1990, *A&A*, 234, 211
 Rizzuti, F., Cescutti, G., Matteucci, F., et al. 2019, *MNRAS*, 489, 5244
 Roederer, I. U., Preston, G. W., Thompson, I. B., et al. 2014, *AJ*, 147, 136
 Salvatier, J., Wiecki, T. V., & Fonnesbeck, C. 2016, *PeerJ Computer Science*, 2, e55
 Schlegel, D. J., Finkbeiner, D. P., & Davis, M. 1998, *ApJ*, 500, 525
 Shipp, N., Drlica-Wagner, A., Balbinot, E., et al. 2018, *ApJ*, 862, 114
 Shipp, N., Li, T. S., Pace, A. B., et al. 2019, *ApJ*, 885, 3
 Sneden, C. A. 1973, PhD thesis, Univ. Texas at Austin
 Sobeck, J. S., Kraft, R. P., Sneden, C., et al. 2011, *AJ*, 141, 175
 Stanford, L. M., Da Costa, G. S., & Norris, J. E. 2010, *ApJ*, 714, 1001
 Tur, C., Heger, A., & Austin, S. M. 2009, *ApJ*, 702, 1068
 Wan, Z., Lewis, G. F., Li, T. S., et al. 2020, *Natur*, 583, 768
 Wanajo, S. 2013, *ApJL*, 770, L22
 Wanajo, S., Müller, B., Janka, H.-T., & Heger, A. 2018, *ApJ*, 852, 40
 Wanajo, S., Nomoto, K., Janka, H. T., Kitaura, F. S., & Müller, B. 2009, *ApJ*, 695, 208
 Wenger, M., Ochsenbein, F., Egret, D., et al. 2000, *A&AS*, 143, 9
 Woosley, S. E., Heger, A., & Weaver, T. A. 2002, *RvMP*, 74, 1015
 Yong, D., Grundahl, F., D'Antona, F., et al. 2009, *ApJL*, 695, L62
 Yong, D., Norris, J. E., Da Costa, G. S., et al. 2017, *ApJ*, 837, 176
 Yong, D., Roederer, I. U., Grundahl, F., et al. 2014, *MNRAS*, 441, 3396